Numerical simulation and experimental study of the damage law of EFP warhead charging of cylindrical shells under different angles

Kun Zhang[a] [iD], Changxiao Zhao[a]* [iD], Chong Ji[a] [iD], Shaoguang Zhang[a] [iD], Xin Wang[a] [iD], Tao Jiang[a] [iD], Gang Wu[a] [iD]

[a] College of Field Engineering, Army Engineering University of PLA, Nanjing 210007, China. E-mail: 513585921@qq.com, 360349734@qq.com, 2468645816@qq.com, 59182874@qq.com, 310433804@qq.com, 254798135@qq.com, 1392520073@qq.com.
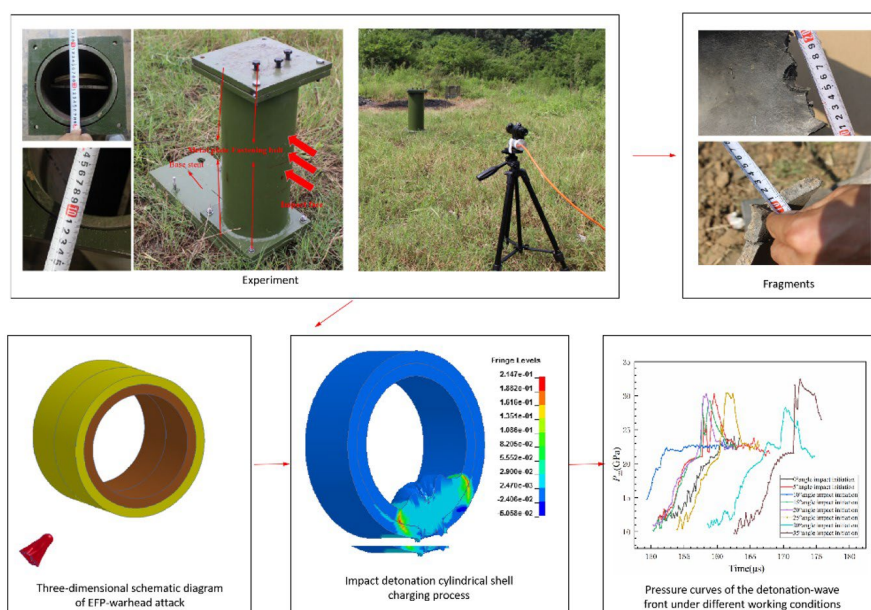
*Corresponding author

Abstract

In this paper, LS-dyna software was used to simulate the charging process of cylindrical shell when EFP has different angles, and some interesting phenomena and laws were found. Cylindrical elastic wave σ_r was generated when the cylindrical shell was impacted by EFP. The cylindrical elastic wave σ_r was correlated with the time required for the cylindrical shell charge to be successfully detonated. When the EFP warhead penetration Angle ϑ ranges from 0° to 10°, the σ_r increases linearly with $(\cos\vartheta)^{-1/2}$. With the increase of ϑ, the tangential velocity v_y had an obvious effect on the impact of EFP on the cylindrical shell, and the linear relationship between the elastic wave σ_r and $(\cos\vartheta)^{-1/2}$ does not change. When the ϑ was greater than 45°, EFP could not successfully impact and detonate the cylindrical shell charge. The EFP velocity was measured by velocity measurement method with an error of 1.3%. The experimental results have strong similarity with the simulation results, indicating that the parameters of the numerical simulation model have good reliability.

Keywords
EFP warhead; Impact detonation; Cylindrical-shell charge; Numerical simulation

Graphical Abstract

Experiment

Fragments

Three-dimensional schematic diagram of EFP-warhead attack

Impact detonation cylindrical shell charging process

Pressure curves of the detonation-wave front under different working conditions

Numerical simulation and experimental study of the damage law of EFP warhead charging of cylindrical shells under different angles

Kun Zhang et al.

1 INTRODUCTION

Explosively formed projectile (EFP) warheads use the principle of energy accumulation to crush the charge cover through the detonation of the explosive, and make it turn over and deform to produce a high-speed and stable flying projectile. EFP have a self-forging projectile structure, and their body structure has a lower velocity than that of the lower tail. It is an efficient damage technology in the field of anti-missile weapon system. Since EFP is insensitive to stand-off distance, it uses a high kinetic energy shock to detonate a low-altitude incoming munition target.

The forming process of EFP is complicated and affected by explosion effect, geometrical shape, material of drug shape cover, charging structure and other factors, EFP design cannot be simplified into a simple and applicable empirical formula. In recent years, the research on EFP in the academic circle can be roughly divided into three categories. The first is the influence of material, structure, explosive and warhead shell on EFP performance (Liu J F.et al., 2017a; Castedo R. et al., 2018 ; Cardoso D. et al., 2016; Liu Y K .et al., 2020); The second is the effect of detonation mode on EFP performance (Zu et al., 2016; Liu J. et al. 2020; Long et al. 2016; Hong et al. 2019); The third category is the research design of EFP with special purpose, including LEFP, circumferential MEFP, coated explosive formed projectiles (CEFP),and so on (Li et al., 2016; Xu et al., 2019; Liang et al., 2019). Zhu et al. (2014) established an analytical model for calculating Mach wave parameters; by changing the diameter of the wave maker and the distance between the wave maker and the liner, he was able to control the pressure and radius of the Mach wave and fit the relationship between the Mach wave and the liner structure. This prevents the front end of the EFP from breaking. Ding et al. (2017) carried out both liner test and flyer plate test experiment, characteristics of a feasible candidate material for EFP liner were discussed. The research results were significant in the material selection of EFP liner especially within high density materials. Hu et al. (2018) conducted series of rigid projectile penetration tests on concrete targets pre-damaged by EFP, discussed the influences of the liner material and configuration of shaped charge, as well as the rigid projectile diameter on the impact performance of two-stage munitions.

EFP impact detonation shell charge is essentially the problem of fragment impact initiation shell charge. According to the public literature reports, the academic circles have also carried out plenty of exploration on the problem of fragmentation impact initiation with shell charge. Guo et al. (2020) comprehensively considered the number of tungsten spheres, spatial collision location distribution and time interval, and obtained the threshold of initiation velocity of cylindrical shell charge through numerical simulation. Yang Y.et al., (2022) used the Lee-Tarver ignition and growth model to study the impact initiation law of double tungsten spheres simultaneously impacting cylindrical shell charge, and found that the pressure peak and duration of superimposed shock wave would both have an impact. Li et al. (2016) used the LS-DYNA finite element software to simulate the process of Linear Explosively Formed Projectile (LEFP) detonating shell charge, and found that LEFP, as an irregular fragment detonated and released charge, has the advantages of large mass, wide contact area, and irregular shape compared with the EFP and shaped charge jet. Li et al. (2020) carried out an experiment on multi-fragment simultaneous-impact initiation and coating of scaled JH-2 high explosives, determined the damage degree of the cover plate by using the Held criterion, and obtained the threshold limit under the impact of multi-fragment and single-fragment conditions; the results showed that the reaction levels of JH-2 HE could be decreased by increasing the number of fragments, the response level using multiple fragment effects is a multiple of a single fragment effect. Xu et al. (2017) studied the response characteristics of Cylindrical Charges Covered with thin Aluminium Shell under the impact of steel fragments at different speeds, and obtained the critical kinetic energy criterion of impact initiation/ignition, through dimensional analysis, the calculation model of critical kinetic energy criterion of impact response was established, which was of great reference significance for the study of impact initiation. As far as authors know, from the published literature, scholars usually adopt idealized regular structural fragments for impact initiation, such as cuboid, cube, sphere, etc., and there is still uncertainty whether the conclusions are applicable to EFP. Therefore, it is worth to construct EFP calculation model for impact initiation of cylindrical shell charge.

In the paper, the simulation of EFP penetrating cylindrical shell charge at different angles was carried out, and the physical parameters of EFP were obtained. The impulse of the Liner element changes exponentially from bottom to edge was found. By adjusting EFP and cylinder shell charge Angle ϑ, the simulation of 45 working conditions was carried out, the influence law of warhead Angle ϑ on EFP impact initiation efficiency was revealed, and theoretical analysis and calculation were carried out by using stress wave theory. The EFP velocity test and the charge test of the impact initiating column shell were conducted. The accuracy of the simulation model and parameters was verified by EFP velocity test and charge test of the impact initiating Cylindrical shell. The results showed that the experimental results were in good agreement with the numerical simulation calculation.

Numerical simulation and experimental study of the damage law of EFP warhead charging of cylindrical shells under different angles

Kun Zhang et al.

2 NUMERICAL CALCULATIONS OF MATERIAL MODEL AND PARAMETER DETERMINATION

2.1 Numerical calculation model

Numerical simulation is carried out using three-dimensional (3D) dynamic finite element program of LS-DYNA in order to study the formation of EFP. The finite element models of the EFP warhead and cylindrical-shell charge investigated this study are shown in Figure 1. The diameter of the warhead was 34 mm and the height of warhead was 50 mm; the shell thickness was 2 mm, and the material used was 6063 aluminum alloy, while the charge was made from 8701 explosive; the material of the Liner was OFHC Cu and adopts the design of variable wall thickness ball shape structure (Liu J F.et al., 2017b; Zhang K.et al., 2020; Zhao C X.et al., 2014). The diameter of the Liner was 30 mm, the radius of internal and external curvature was 38.5 mm and 36 mm respectively, and the wall thickness at the bottom was 2 mm, as shown in Fig 1.

The cylinder shell was made of 45# steel with a thickness of 10 mm, and an outer diameter of 200 mm. In the process of numerical calculation, cylindrical shell charge should be completely filled with cylindrical round tube, but this will lead to an increase in the number of finite element model grids, resulting in a significant increase in the time cost in the process of calculation. In order to give consideration to the calculation effect and the calculation time, the circular charge with a certain thickness is considered in this paper to approximately replace the fully filled dense charge. The two results were highly similar after pre-calculation. In order to save calculation time, all cylindrical shell charges in the subsequent chapters of this study adopt the circular paste charging structure model with the thickness of the charged charge of 10 mm. The EFP warhead was 400 mm vertical from the cylindrical-shell charge. Among the existing ammunition targets, TNT is the majority of internal charge, and TNT sensitivity is relatively small. In order to fully verify the impact initiation ability of EFP, TNT is selected as the embedded inside charge.

In order to reduce the influence of the boundary effect in the process of impact initiation, the length of the one-half finite element model of the cylindrical charge was set at 100 mm. Due to the symmetry of the model, 1/2 of the geometry along the plane of symmetry was established to simplify the calculation. Lagrange formulation was used to keep overlapping in the movement process, which could better track the particle's movement trajectory, observe the detonation pressure change of TNT at any time, and accurately find the critical change moment of the explosive state.

In order to give consideration to the requirements of calculation efficiency and calculation cost, the average size of the explosive and shell elements was 1 mm, the Liner elements was 0.6 mm and cylindrical-shell elements in the impacted area were 0.5 mm, and the other elements of cylindrical-shell elements size was 1 mm in the non-impacted area (Liu et al., 2017b).

The explosive, the shell, and the cylindrical-shell charge models were all divided using the Lagrangian-mesh method with hourglass control, and SOLID164 elements were used for all entity elements in the numerical simulation. In the calculations, it was assumed that the explosive, the shell, and the target plate of the cylindrical shell were uniform continuous mediums, and the whole process of blast penetration was adiabatic and did not consider the influence of gravity. The boundary effect of EFP penetrating cylindrical shell charge was ignored, and the instantaneous global motion of cylindrical shell charge and the influence of air were not considered.

As only a half finite element model was established in this paper, the keyword *BOUNDARY_SPC_SET was used to limit the movement of elements (nodes) on the symmetry plane. After adding this keyword, the displacement and three-dimensional rotational motion of nodes and elements on the symmetry plane were limited. In the process of EFP forming and penetration, there will be violent interaction between explosive and liner, stable forming projectile and each steel target. The *CONTACT_SLIDING_ONLY_PENALTY was used to transfer energy and establish the interaction between 8701 explosive and liner. The interaction between the shaped charge penetrator and the steel target was realized by adding the key word *CONTACT_ERODING_SURFACE_TO_SURFACE (Hallquist J O., 2007). The interaction between the detonation product and the charge cover has no effect after a certain time (Liu et al., 2017b). According to a large number of preliminary estimates, the keyword *DELETE_PART was added to delete the explosive part after 24 μs, and the keyword *DELETE_CONTACT was added to delete the sliding contact between the explosive and the liner, and a small restart calculation was carried out at the same time.
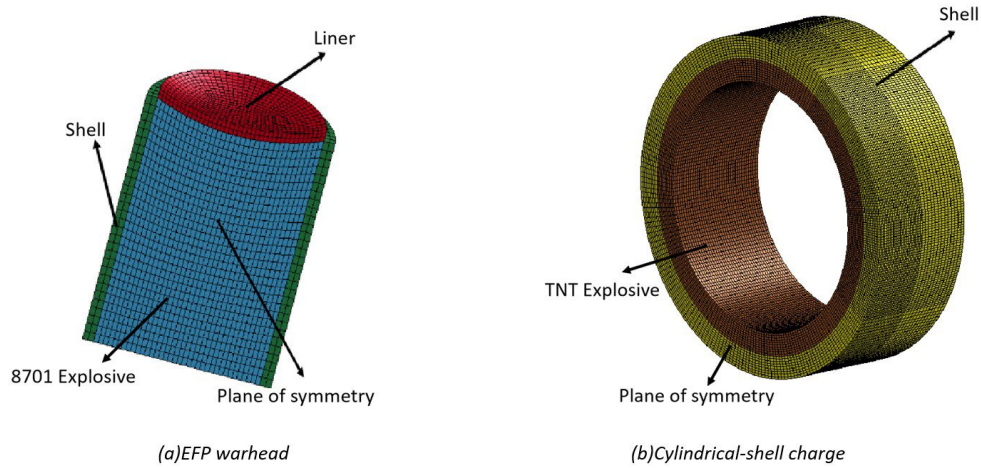
Numerical simulation and experimental study of the damage law of EFP warhead charging of cylindrical shells under different angles

Kun Zhang et al.

(a)EFP warhead   (b)Cylindrical-shell charge

Figure 1: Finite element calculation model

2.2 Material models

Table 1 shows the model parameters of each material and the corresponding physical algorithm. The 8701 explosive charge used *MAT_HIGH_EXPLOSIVE_BURN model, and the state equation was described by *EOS_JWL.The Liner and warhead shell were molded by *MAT_JOHNSON_COOK material model, and the state equation was described by *EOS_GRUNEISEN. The cylinder shell was molded by *MAT_PLASTIC_KINEMATIC material model. Lee-Tarver's trinomial ignition growth equation was used to describe the reaction rate of TNT detonation(Lee and Tarver, 1980, Tarver, 2016). The charged TNT was molded by *MAT_ELASTIC_PLASTIC_HYDRO, and the state equation was described by *EOS_IGNITION_AND_GROWTH_OF_REACTION_IN_HE. The specific meaning of each formula in the physical algorithm and the definition of each letter are shown in the references listed in the Table 1.

Table 1. Material model parameters and algorithms.

Material	Part name	LS-DYNA material type, material property and EOS input data							Physical algorithm
8701 explosive (Wu et al., 2007)	Charge	*MAT_HIGH_EXPLOSIVE_BURN							$p = A(1-\frac{\omega}{R_1 V})e^{-R_1 V} + B(1-\frac{\omega}{R_2 V})e^{-R_2 V} + \frac{\omega E}{V}$
		ρ	D	P_{CJ}					
		1.7 g/cm^3	8315 m/s	29.5 GPa					
		*EOS_JWL							
		A	B	R_1	R_2	ω	V_0		
		8.545	20.49E-2	4.6	1.35	0.25	1.0		
Material	**Part name**	**LS-DYNA material type, material property and EOS input data**							**Physical algorithm**
OFHC-Cu (Liu et al., 2017b)	Liner	*MAT_JOHNSON_COOK							$\sigma_y = \left(A_1 + B_1(\overline{\varepsilon}^p)^n\right)\left(1 + C\ln\dot{\varepsilon}^*\right)\left(1-(T^*)^m\right)$
		ρ	G	A_1	B_1	C	m	T_m	$p = \frac{\rho_0 C_1^2 \mu\left[1+\left(1-\frac{\gamma_0}{2}\right)\mu - \frac{a}{2}\mu^2\right]}{\left[1-(S_1-1)\mu - S_2\frac{\mu^2}{\mu+1} - S_3\frac{\mu^3}{(\mu+1)^2}\right]} + (\gamma_0 + \alpha\mu)E$
		8.96 g/cm^3	46 GPa	0.9E-3	2.92E-3	0.025	1.09	1356 K	
		*EOS_GRUNEISEN							
		C_1	S_1	S_2	S_3	γ_0	α		
		0.394	1.489	0	0	2.02	0.47		
Material	**Part name**	**LS-DYNA material type, material property and EOS input data**							**Physical algorithm**
6063 aluminum alloy	Warhead shell	*MAT_JOHNSON_COOK							$\sigma_y = \left(A_1 + B_1(\overline{\varepsilon}^p)^n\right)\left(1 + C\ln\dot{\varepsilon}^*\right)\left(1-(T^*)^m\right)$
		ρ	G	A_1	B_1	C	m	T_m	
		2.7 g/cm^3	27.6 GPa	2.65E-3	4.26E-3	0.015	1.09	775 K	
		*EOS_GRUNEISEN							
		C_1	S_1	S_2	S_3	γ_0	α		
		0.5328	1.338	0	0	2.0	0		
Material	**Part name**	**LS-DYNA material type, material property and EOS input data**							**Physical algorithm**
45# steel (Wu et al., 2007)	cylinder shell	*MAT_PLASTIC_KINEMATIC							$\sigma_Y = \left[1+\left(\frac{\dot{\varepsilon}}{C}\right)^{1/p}\right]\left(\sigma_0 + \beta E_P \varepsilon_p^{eff}\right)$
		ρ	E	μ	σ_s	E_t	ε_s		
		7.83 g/cm^3	207 GPa	0.3	0.005	207 MPa	0.47		
Material	**Part name**	**LS-DYNA material type, material property and EOS input data**							**Physical algorithm**
TNT explosive (Jiang, 2006)	Charge	*MAT_ELASTIC_PLASTIC_HYDRO							$\dot{F} = I(1-F)^b(\rho/\rho_0 -1-a)^x + G_1(1-F)^c F^d P^y + G_2(1-F)^e F^g P^z$
		ρ	A	B	R_1	R_2	ω		
		1.65 g/cm^3	171.01	-0.03745	9.8	0.98	0.5647		

Numerical simulation and experimental study of the damage law of EFP warhead charging of cylindrical shells under different angles

Kun Zhang et al.

3 NUMERICAL RESULTS AND ANALYSIS

3.1 Numerical simulation of the EFP forming process

An EFP is the result of the self-forging deformation of a concave metal hood driven by a detonation wave and detonation product. Figure 2 shows the forming process of an EFP, which records the typical states of the EFP at different moments after the central point at the bottom of the warhead was detonated.

| t=28μs | t=70μs | t=120μs | t=130μs |
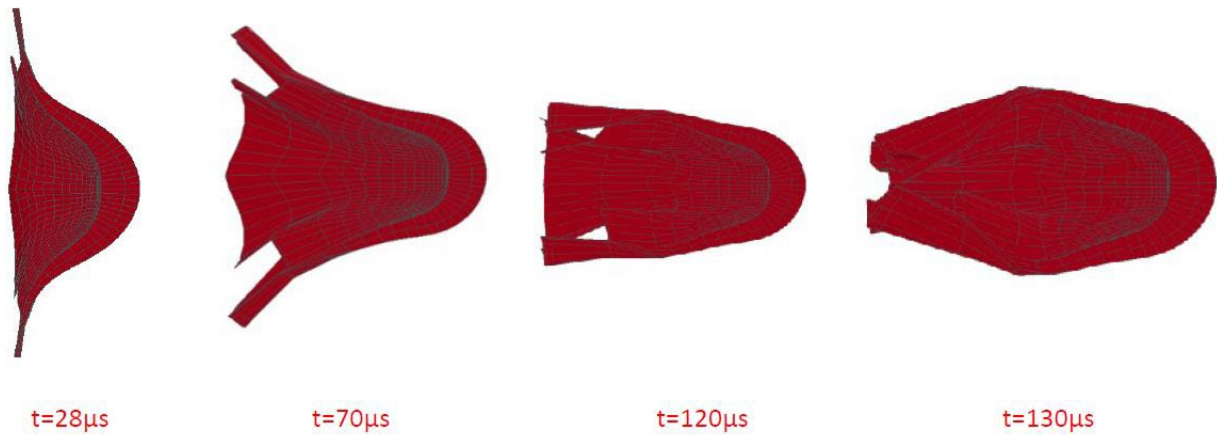
Figure 2: Several typical states of EFP forming process

Table 2. EFP performance parameters at 130 μs

parametric	m/g	l/cm	λ	d/cm	v_t/(m/s)	v_w/(m/s)
parameter	5.9	2.93	2.46	1.19	1710	1710

At the time of 130 μs, the projectile tended to be stable, and the morphological characteristics no longer changed. In Table 2, m is the mass of the projectile, L is the length, λ is the length–diameter ratio, D is the diameter, and v_t and v_w are the head velocity and tail velocity, respectively. The final shape of the EFP mainly depended on the velocity distribution of each element on the concave metal hood. The concave metal hood was divided into micro-elements with equal mass, and the micro-elements not in the same torus had different crushing velocities. The interaction between the micro-elements of concave metal hood was ignored in the crushing process. Seven observation points with equal spacing were selected on the Liner cover. The center points at the bottom of the Liner cover were #791, #761, #731, #701, #998, #995, and #992 along the axial direction, as shown in Figure 3. It can be seen from Figure 4 that the closer the observation point was to the central axis of the charge cover, the greater the velocity was. Conversely, the farther away from the central axis, the lower the velocity was. When the whole projectile tended to be stable, its morphological characteristics no longer changed, and the velocity of each element along with other parameters remained constant.
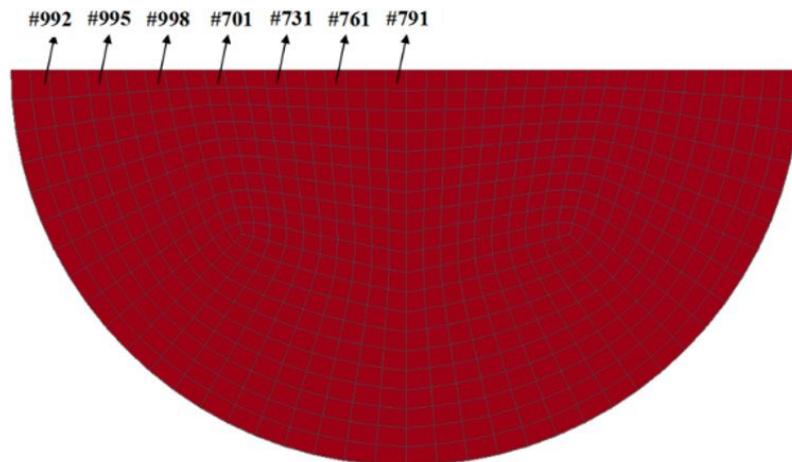

Figure 3: Distribution diagram of observation points

Numerical simulation and experimental study of the damage law of EFP warhead charging of cylindrical shells under different angles
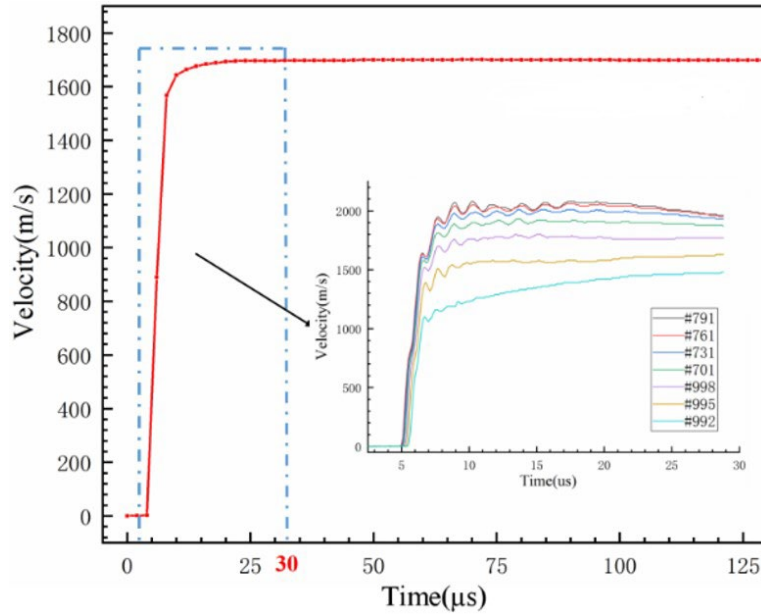
Kun Zhang et al.

Figure 4: Projectile velocity curve and observation point velocity curve

Taking the detonation surface of each observation point as a unit area, the total impulse was calculated by integrating the impact pressure at each point. Figure 5 shows the histogram of the impulse distribution of the observation points under the action of the detonation wave. It can be seen that the closer the observation point was to the axis, the greater the impulse; when farther away from the axis, the impulse decreased significantly. In order to further analyze the variation rule of the impulse values at each observation point, the ratio of the impulse values at observation point #791 to the value at the other observation points was defined as γ, and finally the dimensionless impulse ratios of the seven groups were obtained. Figure 6 shows the distribution of the impulse ratio γ. By fitting the impulse ratio γ to a curve, an exponential function can be obtained as shown in Equation (1). The correlation index of the fitting curve was 0.9943, and x represented the dimensionless spacing ratio between the remaining points and the innermost point #791, which was defined as the proportional spacing. By comprehensive analysis, it was found that the impulse ratio of each element along the radial direction of the charge cover attenuated in the form of approximate exponent:

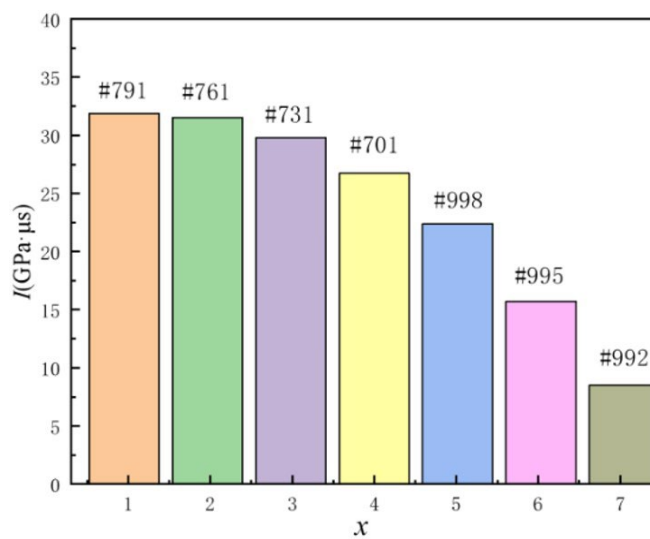$$\gamma = 1.00595 + 0.00326e^{0.96177x} \tag{1}$$

Figure 5: Impulse distribution of observation points

Numerical simulation and experimental study of the damage law of EFP warhead charging of cylindrical shells under different angles
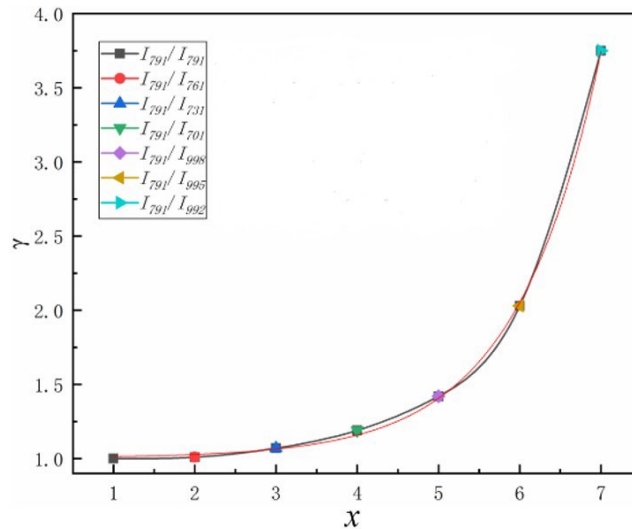
Kun Zhang et al.

Figure 6: Ratio of the impulse received by #791 to the impulse received at other points

3.2 EFP impact penetration when perpendicular to the charge axis of the shell

Considering the external characteristics of the cylindrical-shell charge, EFP-warhead oblique-impact penetration is a common target attitude. This section mainly studies the impact-initiation characteristics of an EFP warhead and cylindrical-shell charge under different angles when the charge axes are perpendicular to each other and discusses the impact-initiation efficiency of cylindrical-shell charges under different angles. The physical model of the EFP warhead acting on the cylindrical-shell charge and the attack diagram of the EFP warhead are shown in Figures 7 and 8. Here, the EFP-warhead acting direction was perpendicular to the charge axis.
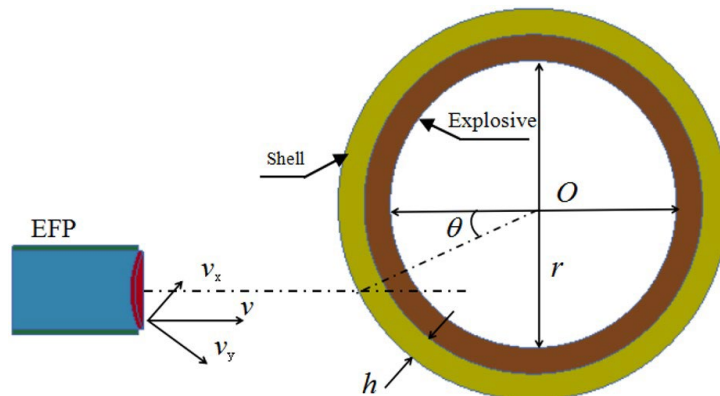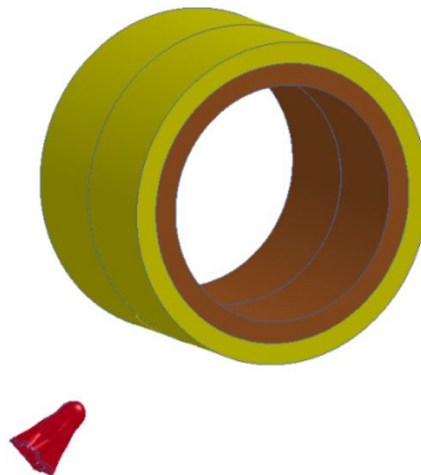

Figure 7: Diagram of EFP-warhead attack profile

Figure 8: Three-dimensional schematic diagram of EFP-warhead attack

Numerical simulation and experimental study of the damage law of EFP warhead charging of cylindrical
shells under different angles

Kun Zhang et al.

The range of the EFP-warhead angle ϑ varied from 0° to 45°, and a numerical-calculation condition was set at every 1° interval. Each condition was counted as a working condition and was numbered 1 to 46 in order. The impact-initiation performance of the EFP warhead against a cylindrical-shell charge at different angles was analyzed by numerical calculation under the 46 working conditions. According to the numerical results, when the angle ϑ increased to 36°, the projectile could no longer impact the charge of the priming-column shell (see Table 3 for details), and when angle ϑ increased to 40°, the projectile would jump off.

Table 3. The 46 calculation conditions and distribution of impact-initiation results

Calculated	1	2	......	35	36	......	45
Angle ϑ(°)	0	1	......	36	37	......	46
Results	Initiating	Initiating	......	Initiating	No initiating	......	No initiating

The impact-initiation process of the projectile on the cylindrical-shell charge was studied by taking the projectile-landing angle of 15° as an example under working condition 16. According to the numerical calculation and impact-initiation theory, the projectile impact-initiation cylindrical-shell charging process can be divided into three stages. In the first stage, the EFP head impinges on the steel shell at high speed, forming a plastic-deformation zone and a high-pressure zone around the impact point, and generating a strong shock wave on the projectile head. With the increase of penetration depth, the EFP residue will undergo violent plastic flow along the bottom of the crater to the crater entrance, as shown in Figures 9(b) and (c). During the second stage, the shock wave and stress wave generated by the EFP impacting the steel shell continue to propagate and are incident on the inside of the charge on the back of the shell, accompanied by the reflection and transmission of the complex wave system. The shock wave compacts the explosive adiabatically, and the temperature of the explosive increases rapidly after the overall shock compression, causing a chemical reaction to occur when it reaches a certain threshold. Local areas under the combined action of the shock wave and chemical reaction are the first to detonate, as shown in Figure 9(c). Finally, in the third stage, the chemical reaction propagates to the unreacted area at a greater speed, and the energy released strengthens the initial shock wave. When the detonation wave catches up with the incident shock wave, the two act together inside the charge and eventually develop into a stable detonation, as shown in Figure 9(d).

(a)t=128μs

(b)t=136μs

(c)t=170μs

(d)t=175μs
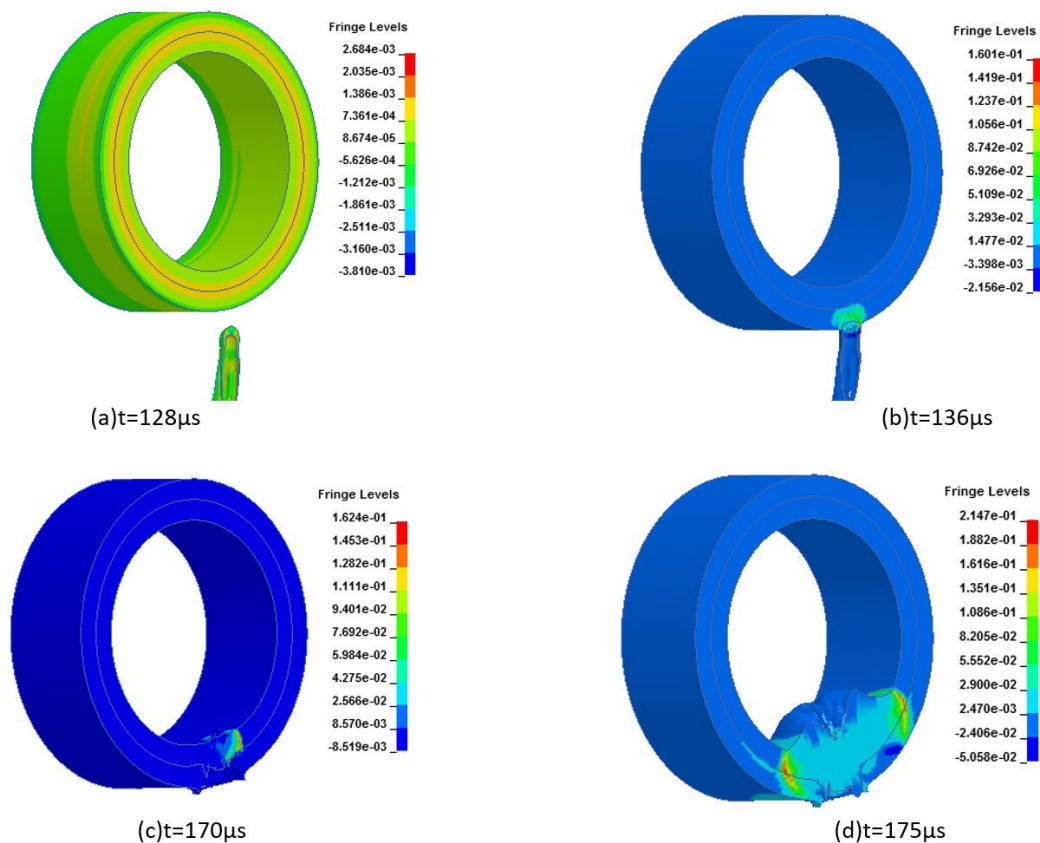
Figure 9: The process of penetration into the cylindrical shell and initiation charge when the impact angle is 15°

Numerical simulation and experimental study of the damage law of EFP warhead charging of cylindrical shells under different angles

Kun Zhang et al.

In the peak-pressure curve of the detonation-wave front of the charge recorded in Figure 10, the moment when the projectile penetrates the steel shell was selected as the initial moment to start recording. When the EFP penetrated the steel shell at 150.2 μs, the internal peak pressure of the charged TNT was only 1.91 GPa, which was far lower than the critical detonation pressure of 10.4 GPa (Tang et al. 2004, Zhang G R.et al. 1991). The remaining projectiles and the fallen steel-shell fragments continued to impact and compress the TNT, and the peak pressure inside the TNT at 152.8 μs was 10.6 GPa, which exceeded the critical detonation pressure. The TNT was detonated by impact and gradually developed into a stable detonation. The impact angle of the EFP warhead determined the impact position of the projectile. The change of the impact angle meant that the impact position was different, and the impact-initiation phenomenon changed simultaneously. As the angle increased, the interaction distance between the projectile and the steel shell increased. The projectile in the first working condition (vertical penetration) acted on the steel shell first, and the other working conditions acted on the steel shell successively.
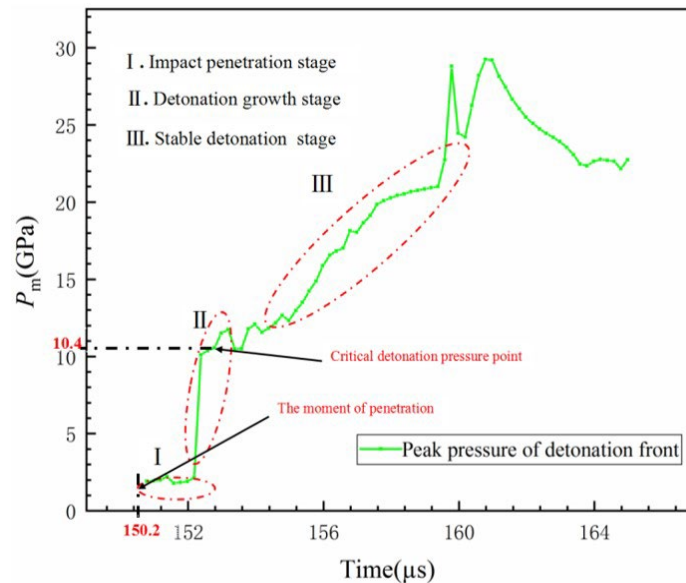

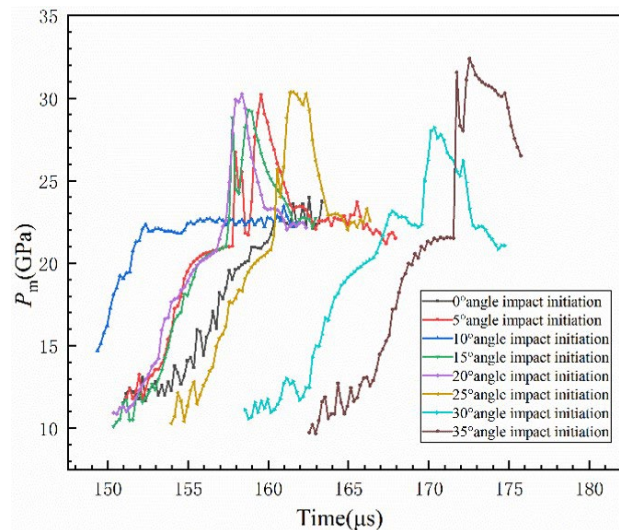**Figure 10:** Pressure curve of the detonation-wave front under working condition 16

Figure 11: Pressure curves of the detonation-wave front under different working conditions

A calculation condition was selected for analysis every 5° starting with vertical penetration (landing angle of 0°). Figure 11 shows the pressure-change curve of the impact-initiation charge at different positions of the shell when a projectile with the same body parameters hit the shell. As shown in the figure, in working condition 1 (vertical penetration), the detonation pressure of TNT after the impact penetration continued to rise and finally stabilized at 22.1-22.8 GPa. According to the detonating theory of explosives, the peak pressure of the C-J plane during the TNT detonation was 19-21 GPa. The numerical simulation results were in good agreement with the theoretical calculation, which further

Numerical simulation and experimental study of the damage law of EFP warhead charging of cylindrical shells under different angles

Kun Zhang et al.

confirmed that the TNT was successfully impacted and the detonation was stable. Working condition 6 (attack angle of 5°,the same below) turned into strong detonation after a short stable-detonation stage, and the peak pressure of the wave front jumped to 30.2 GPa. After that, the detonation pressure dropped and returned to a stable-detonation state. Among all of the working conditions, working condition 11 was the first to enter the stable-detonation state, and the peak pressure was 22.3-22.5 GPa. Working conditions 6 , 11 , 16 , and 21 all entered the detonation state earlier than working condition 1 (vertical penetration), indicating that the impact-initiation ability of the four working conditions was significantly better than that of working condition 1 (vertical penetration). Although detonation characteristics also appeared in working conditions 31 and 36, the preliminary process of explosive detonation formed under impact action was obviously longer than that in other working conditions, indicating that the projectile impact-initiation ability was weakened. There was no impact initiation for the cylindrical-shell charge under working conditions 37-46.

The comprehensive analysis of impact-initiation characteristics under the 46 working conditions was obtained as follows:

(1) In this example, vertical penetration does not have the optimal impact-initiation ability. When the angle of impact ϑ is 10°, the first impact-initiation charge is detonated, and stable detonation is formed. In the range of impact angles ϑ from 0° to 35°, the projectile impact-initiation ability increases first and then decreases with the increase of the angle.

(2) In Figure 11, except for working condition 11, the charges in the other working conditions all present the characteristics of temporary strong detonation. The main reason for this phenomenon is that after the shell is penetrated by the projectile, the projectile residual body and the shell debris jointly impact the charges, and under this action, the local hot spots of the charges rapidly increase, presenting the phenomenon of temporary strong detonation.

(3) In this example, when the angle of impact is greater than 36°, the initiation-column shell charge cannot be impacted, but when the angle ϑ is greater than 40°, the projectile will jump off when it impacts and impinges into the cylindrical-shell charge, as shown in Figure 12.
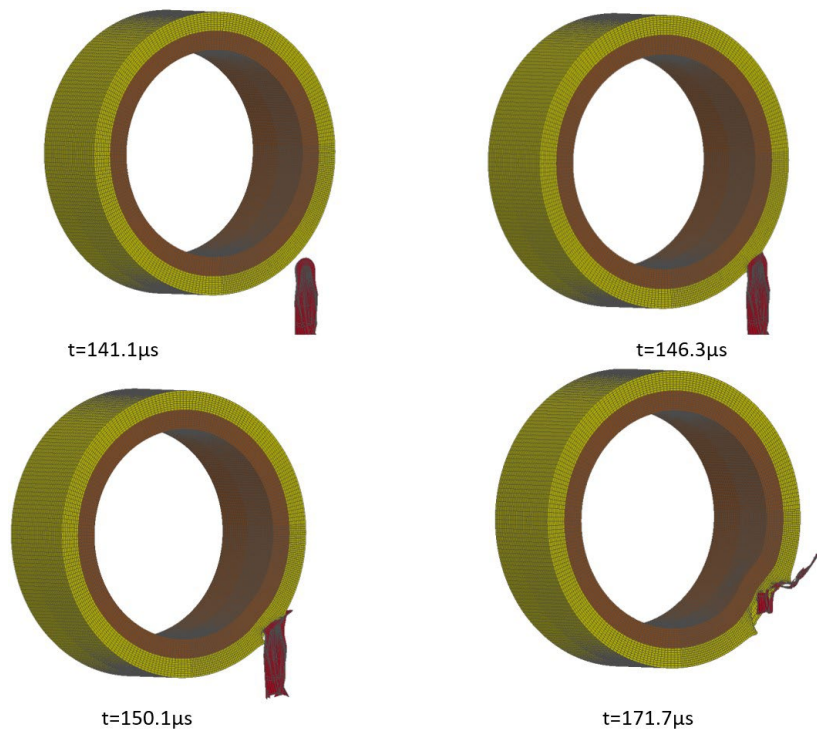

t=141.1μs

t=146.3μs

t=150.1μs

t=171.7μs

Figure 12: Projectile-impact process on the cylindrical-shell charge at an angle of 40°

3.3 Analysis of the law of impact angle on the projectile impact-initiation efficiency

The EFP caliber studied in this work was negligible compared with the diameter of the cylindrical shell. The projectile impact and penetration into the cylindrical shell was a point-impact problem, and the load generated was a highly-localized impact load. The cylindrical-shell charge belonged to the cylindrical-cavity wall structure. Compared with the plane wave, the cylindrical wave generated by the impact and penetration diffused, and the wave profile changed constantly.
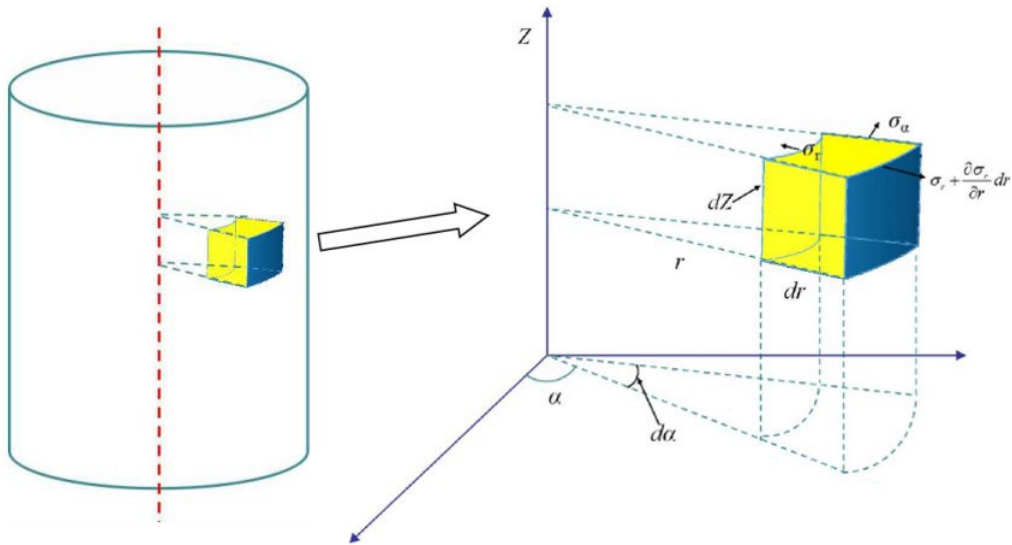
Numerical simulation and experimental study of the damage law of EFP warhead charging of cylindrical shells under different angles

Kun Zhang et al.

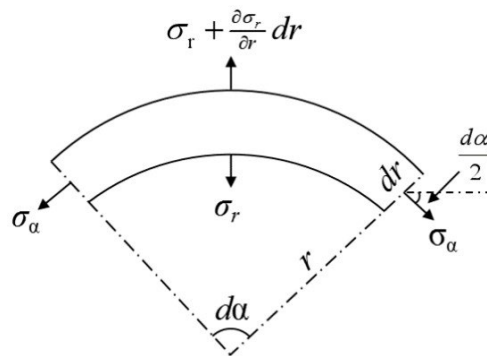**Figure 13:** Schematic diagram of an element in Lagrange cylindrical coordinates

Figure 14: Sectional view of the inclusions of the columnar coordinates r and α.
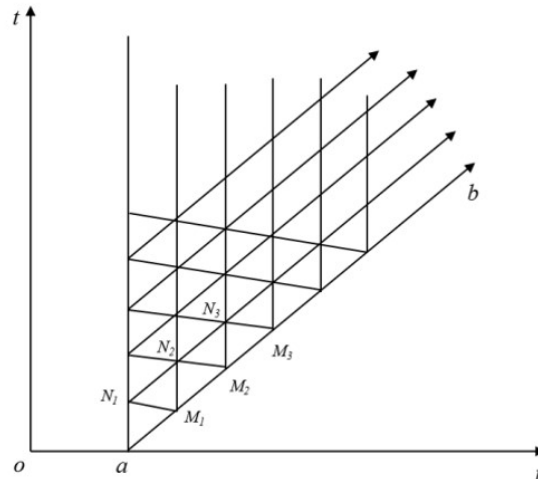

Figure 15: Distribution of wave characteristic lines on an elastic cylinder.

The wave front formed by the EFP impacting cylinder shell charge is a radial cylindrical wave. Due to the motion-column symmetry properties of the medium, only the radial displacement component $u(r, t)$ was a non-zero-displacement component in Lagrangian cylindrical coordinates (as shown in Figures 13 and 14), and each state parameter was only a function of column diameter r and time t, independent of both α and Z. ρ_0 represented the density cylinder. Hence, we had the following formula:

Numerical simulation and experimental study of the damage law of EFP warhead charging of cylindrical shells under different angles

Kun Zhang et al.

$$\varepsilon_r = \frac{\partial u}{\partial r} \tag{2}$$

$$v = \frac{\partial u}{\partial t} \tag{3}$$

$$\varepsilon_\alpha = \frac{u}{r}, \ \varepsilon_Z = 0 \tag{4}$$

$$\sigma_r = \sigma_r(r,t), \ \sigma_\alpha = \sigma_\alpha(r,t), \ \sigma_Z = \sigma_Z(r,t) \tag{5}$$

To ensure that the displacement $u(r,t)$ was a single-valued continuous function of r and t, the following compatibility conditions needed to be satisfied between the strain and the radial velocity:

$$\frac{\partial \varepsilon_r}{\partial t} = \frac{\partial v}{\partial r} \tag{6}$$

$$\frac{\partial \varepsilon_\alpha}{\partial t} = \frac{v}{r} \tag{7}$$

The above equation is the continuity equation in the governing equations of the cylindrical wave, which represents the condition of mass conservation.

According to the momentum conservation condition in the radial direction,

$$\left(\sigma_r + \frac{\partial \sigma_r}{\partial r} dr \right)(r+dr)d\alpha - \sigma_r r d\alpha - 2\sigma_\alpha \sin\frac{d\alpha}{2}\left(r + \frac{dr}{2} \right) = \rho_0 \left(r + \frac{dr}{2} \right) \ d\alpha dr \frac{\partial v}{\partial t} \tag{8}$$

By expanding the above equation and ignoring the small quantities of higher order, we can obtain

$$\frac{\partial \sigma_r}{\partial r} + \frac{\sigma_r - \sigma_\alpha}{r} = \rho_0 \frac{\partial v}{\partial t} \tag{9}$$

Equations (10) and (11) represent the continuity equation of the radial-cylindrical wave, and Equation (13) is the motion equation. Due to the extremely complex problem of the wave caused by the projectile impact and penetration, to simplify the calculation, only the cylindrical-wave propagation law in the material with a linear elastic-constitutive relation for a fixed cylindrical wave was considered.

On the premise of the above equation, the generalized Hooke's law given in the form of a capacitive variation and distortion rate can be reduced to

$$\sigma_r + \sigma_\alpha + \sigma_z = 3K(\varepsilon_r + \varepsilon_\alpha) \tag{10}$$

$$\sigma_r - \sigma_\alpha = 2G(\varepsilon_r - \varepsilon_\alpha) \tag{11}$$

$$\sigma_r - \sigma_\alpha - 2\sigma_Z = 2G(\varepsilon_r + \varepsilon_\alpha) \tag{12}$$

where K is the volume modulus and G is the shear modulus.

For a cylindrical-radial wave, the governing equations consist of six equations, namely, Equations (6), (7), and (9)-(12). Six unknown functions, namely, σ_r, σ_α, ε_r, ε_α, v, and σ_Z, are then able to be solved.

When the characteristic-line method is used to solve the elastic cylindrical-wave problem, the eigen-compatibility relation should be introduced. This can then be simplified to the following expression:

$$dr = \pm C_L dt \tag{13}$$

Numerical simulation and experimental study of the damage law of EFP warhead charging of cylindrical shells under different angles

Kun Zhang et al.

$$d\sigma_r = \pm\rho_0 C_L dv - 2\left[(\sigma_r - \sigma_\alpha) \mp (K - \frac{2G}{3})\frac{v}{C_L}\right]\frac{dr}{r} \tag{14}$$

where CL represents the propagation speed of the boundary loading. Equation (13) describes the propagation paths of positive and negative wave fronts of the two families of characteristic lines as well as the corresponding characteristic-compatibility relations. Equation (14) provides the mutual-restriction relations among σ_r, σ_α, and v in the process of disturbance propagation, so as to ensure that continuity conditions, momentum-conservation conditions, and material-constitutive relations are satisfied. It should be pointed out that, compared with the eigen-compatibility relation of one-dimensional strain-plane waves, there are more dr/r-related terms in Equation (14), which represent the cylindrical-diffusion characteristics of cylindrical waves. As r goes to infinity, this term tends towards zero and becomes a one-dimensional strain-plane wave problem.

The initial conditions and boundary conditions are set to $u(r, 0) = v(r, 0) = \sigma_r(r, 0) = \sigma_\alpha(r, 0)$, and $\sigma_r(a, t) = -P_0$ for ($a<r\leq\infty$, $t\geq0$). This is a cylindrical wave-propagation problem when a constant pressure P_0 is applied to the cylinder wall of a medium that was previously in a static and undisturbed state. Assuming that P_0 is insufficient to cause plastic deformation, strongly-discontinuous radial-cylindrical waves will propagate along the characteristic AB with Cl wave velocity, and the propagation along AB will also satisfy Equation (14). Considering that along the AB line, as shown in Figure 15, the displacements should be continuous, then $\varepsilon_\alpha = u/r = 0$, and the following equation can be deduced from Equation (11) (Wang L L.et al., 2005; Timoshenko S.et al., 1951; Selberg H L. 1952):

$$\sigma_r = -\sqrt{\frac{a}{r}}P_0 \tag{15}$$

$$v = \sqrt{\frac{a}{r}}\frac{P_0}{\rho_0 C_L} \tag{16}$$

$$\sigma_\alpha = \sigma_Z = -\frac{\upsilon}{1-\upsilon}\sqrt{\frac{a}{r}}P_0 \tag{17}$$

According to the above equation, the stress amplitude σ_r of the strongly-discontinuous cylindrical-elastic wave decreases inversely with $\sqrt{r}$ with the increase of the distance from the center of the axis. On the contrary, if the elastic wave gathers and propagates toward the center of the column (agglomeration), the stress amplitude σ_r increases, which will lead to convergent detonation.
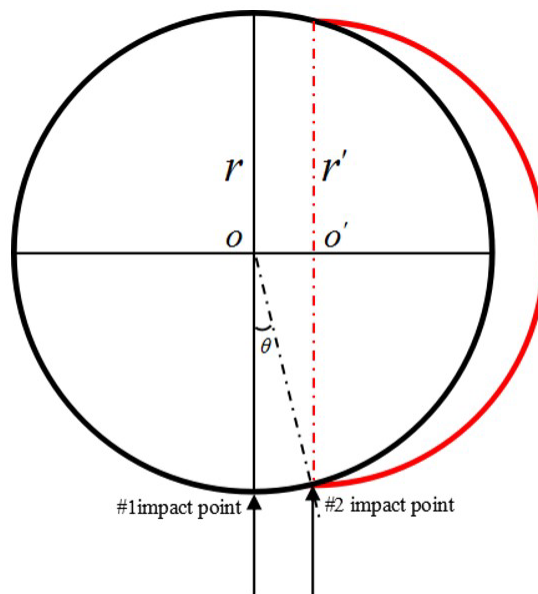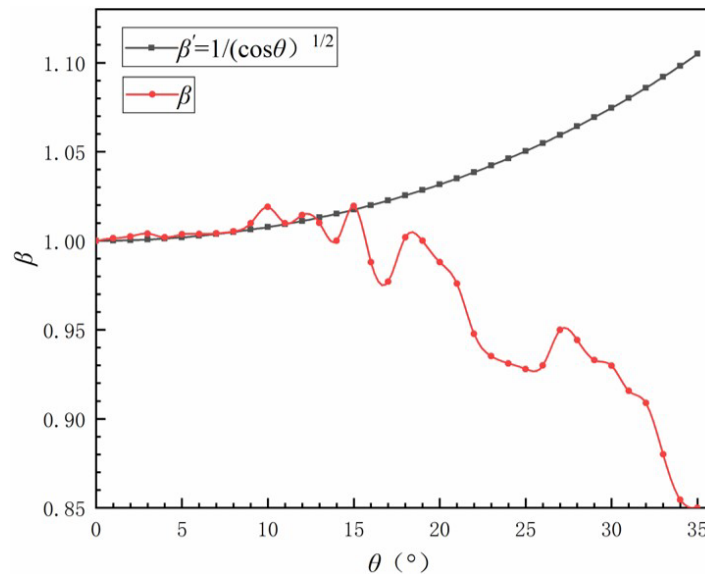

Figure 16: Projectile-impact point and effective cylindrical-shell radius distribution

Numerical simulation and experimental study of the damage law of EFP warhead charging of cylindrical shells under different angles

Kun Zhang et al.

Figure 17: Ratio curve of effective impact-action time between working condition 1 and other working conditions

In this case, the projectile-impact cylindrical shell is a highly-localized point-impact problem. When the impact angle of the projectile is changed, an eccentricity between the projectile and the cylindrical shell will occur. At this time, the effective cylindrical-shell radius corresponding to the impact point can be approximated as $r' = r\cos\theta$, as shown in Figure 16. According to the above equation, at this point $\sigma_r = -\sqrt{\dfrac{a}{r\cos\theta}}P_0$; that is, the stress σ_r has a linear relationship with $1/\sqrt{\cos\theta}$. When angle ϑ increases within a certain range, the effective shell radius r' decreases, and σ_r increases accordingly.

To analyze the difference in projectile impact-initiation efficiency in various working conditions in detail, $\Delta t = t_2 - t_1$ was defined. Δt was the effective impact-action time of the projectile, t_1 was the contact time between the projectile and the outer surface of the cylindrical-shell charge, and t_2 was the time when the fired charge reaches stable detonation (the stable-detonation pressure was 21.3 GPa). The ratio of the effective impact time of the projectile in the recorded working condition 1 (vertical penetration) to the other working conditions was carried out, and the result was recorded as β.

However, the application scope of the aforementioned idea of an effective shell radius is limited. With the increase in angle ϑ, the effect of tangential velocity v_y on the projectile impacting the shell can no longer be ignored. Because the tangential velocity increases rapidly, the projectile impact-initiation efficiency decreases rapidly. As the angle continues to increase, the vertical velocity v_x of the projectile decreases rapidly and becomes lower than the critical initiation velocity. The mass and kinetic energy of the projectile decay rapidly, and the projectile cannot impact the initiation cylindrical charge, and so the projectile jumps away. The red curve in Figure 17 was obtained by fitting the ratio of effective impact time of the projectile in working condition 1 to the other working conditions, and the black curve is the function $\beta' = 1/\sqrt{\cos\theta}$. In conclusion, for this example, when angle $\vartheta \in [0°, 10°]$, the change law of β' and β had a good consistency, which indicated that when the projectile impacted on the cylindrical-shell charging target in this angle interval, the impact initiation ability of the projectile on the cylindrical-shell charging target changed with the approximate relationship of $1/\sqrt{\cos\theta}$ with the angle ϑ.

4 TEST EQUIPMENT AND LAYOUT

4.1 Velocity test of EFP-warhead projectile

The EFP-warhead assembly was composed of a shell, concave metal hood, and explosive, among other components. The caliber of the EFP warhead was 34 mm, and the height was 50 mm. The shell thickness was 2 mm, and the material was 6063 aluminum alloy. The warhead charge was made from 8701 explosive. The material of the Liner was OFHC-Cu with a spherical structure with variable wall thickness. The diameter of the liner was 30 mm, the radii of internal and external curvature were 38.5 mm and 36 mm, respectively, and the bottom wall thickness was 2 mm, as shown in Figure 18.
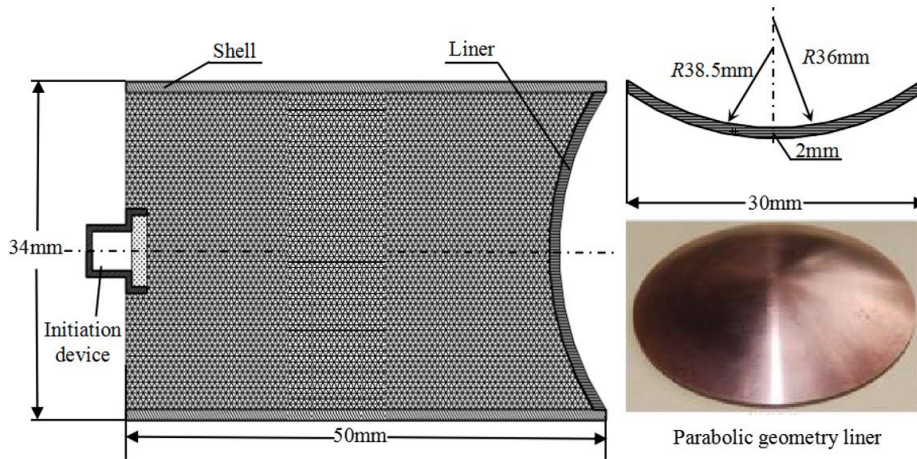
Numerical simulation and experimental study of the damage law of EFP warhead charging of cylindrical shells under different angles

Kun Zhang et al.

Figure 18: EFP warhead structure prepared

An electronic chronometer was used to measure the speed of the EFP in stable flight after forming. The main test setup consisted of two parts: the zone-cutting device and electronic chronometer. Two target boards constituted a zone-cutting device, and each target board was provided with two layers of insulating tin-foil paper. The basic principle was to determine the distance between the two target plates, and then when the projectile passed through the two target plates, the average velocity of the projectile could be calculated using the electronic-timing instrument. The test settings are shown in Figures 19 and 20.
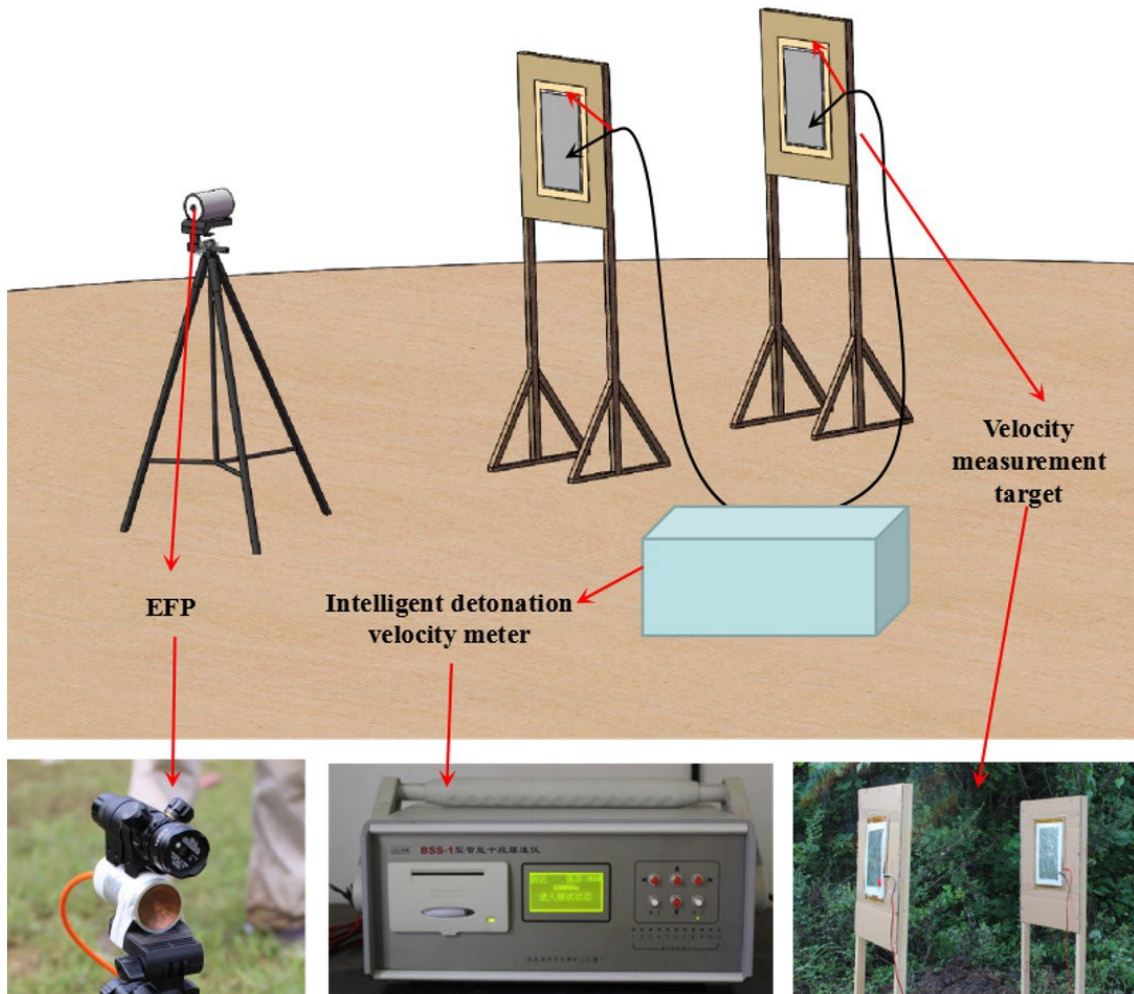

Figure 19: Schematic diagram of the EFP speed-test settings

Numerical simulation and experimental study of the damage law of EFP warhead charging of cylindrical shells under different angles

Kun Zhang et al.

Figure 20: Settings of two velocity targets

The instrument used for the velocity test was a BSS-1 Intelligent Ten Section Detonation Velocity Instrument. Three groups of velocity-measurement tests were carried out. Three distances between the No. 1 and No. 2 targets L_2 were set as 1000 mm, 2000 mm, and 3000 mm, and the communication number time t_c of the two targets collected by the electronic-timing instrument when the projectile penetrated the No. 1 and No. 2 targets was recorded. The specific results are shown in Table 4. The average velocity of the EFP was 1688 m/s through the three groups of tests. The EFP velocity obtained from the numerical simulation was 1710 m/s, and the error between the test results and the numerical-simulation results was -1.3%. This indicated that the test results were in good agreement with the simulation results, and the numerical-simulation results had high reliability.

Table 4. EFP velocimetry test results record

Exp		1	2	3
Test results	L_2/cm	100	200	300
	t_c/μs	595.2	1177.4	1780.1
	v/m·s^{-1}	1680.1	1698.7	1685.3
Parameter comparison		v(m·s^{-1})		
	Exp.		Sim	Error(%)
	1688		1710	−1.3

4.2 Verification and analysis of EFP warhead impact damage effectiveness

On the basis of verifying the velocity of the EFP-warhead projectile, a charging test of the impact-initiation column shell was conducted. Figures 21 and 22 show the specific settings used. The EFP warhead equipped with a sighting instrument was fixed on the tripod, and the simulated target for the cylindrical shell charge was placed along the EFP trajectory line 5000 mm away from the warhead. The EFP warhead was used to simulate the vertical action of the UXO target with a laser sight (the angle of impact ϑ was 0°). The size of the simulated target was the same as that of the numerical simulation; the length was 500 mm, the diameter was 200 mm, the shell thickness was 10 mm, and the internal charge was powdered TNT. After filling the simulated target with powdered TNT, the TNT explosive was compacted layer by layer, and then the upper cover plate was added and fixed with bolts. To ensure the stability of the simulated target, its bottom was fixed on a rectangular steel base. There were three explosion-proof monitors in the test site, which could record the test status from multiple perspectives.
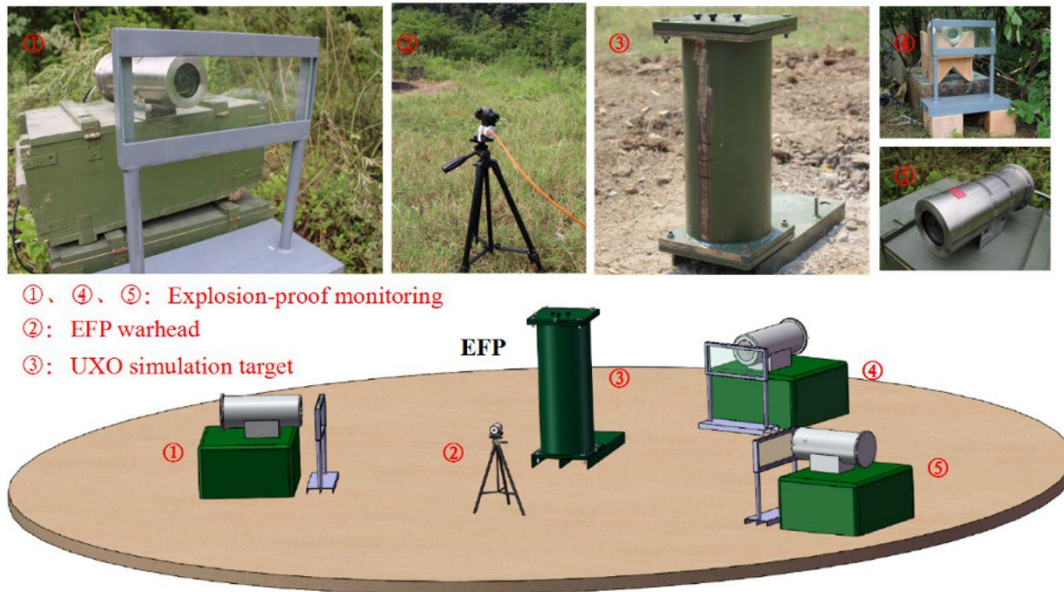
Numerical simulation and experimental study of the damage law of EFP warhead charging of cylindrical shells under different angles

Kun Zhang et al.

Figure 21: Schematic diagram of the simulated cylindrical shell charge target detonated by warhead impact

Figure 22: Test settings of the simulated target and EFP-warhead impact detonating simulated target

Figure 23 shows the simulated-target process of the EFP damage element impacting and detonating the 10-mm thick cylindrical shell charge at a distance of 500 cm recorded by the explosion-proof monitoring. At *t*=2.88 ms, the simulated target was successfully detonated by impact, accompanied by a strong fire and shock wave. Under the combined action of the shock wave and detonation-reaction products, the shell of the simulated target was blasted and dispersed to the surroundings. At *t*=2.98 ms, the air-defense monitoring captured the moment when the simulated-target shell fragment flew out. The lower-right part of the figure shows the final test site and the recovered shell fragments, which fully indicated that the 10-mm thick simulated target was successfully detonated by the EFP warhead. The test results and numerical-simulation results could be mutually verified.

Fragments after the explosion of cylindrical shell charge were recovered, shown as Figure 24. The aperture of projectile penetration cylindrical shell was measured to be 27mm, and the aperture of penetration obtained by numerical simulation was 29mm, with an error of 6.89%, indicating that the numerical calculation had a good consistency with the test.
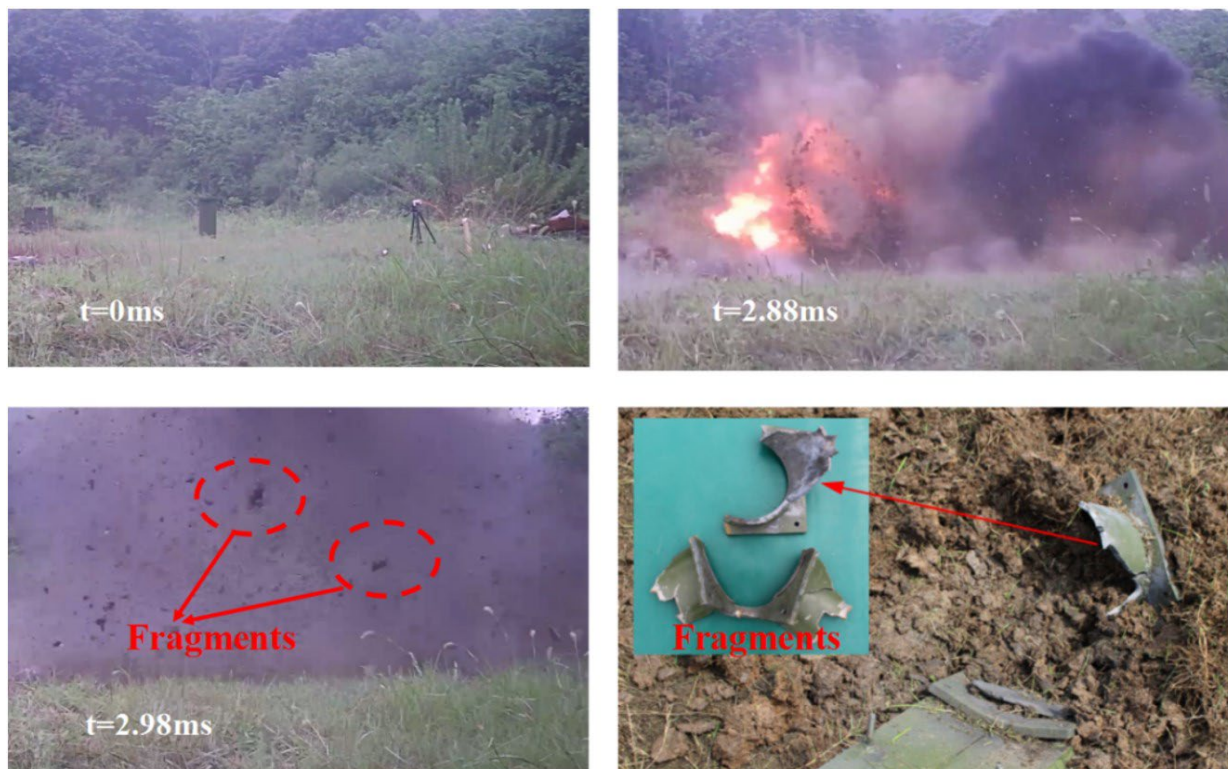
Numerical simulation and experimental study of the damage law of EFP warhead charging of cylindrical shells under different angles

Kun Zhang et al.

Figure 23: EFP-warhead impact detonation of 10-mm thick simulated-target process
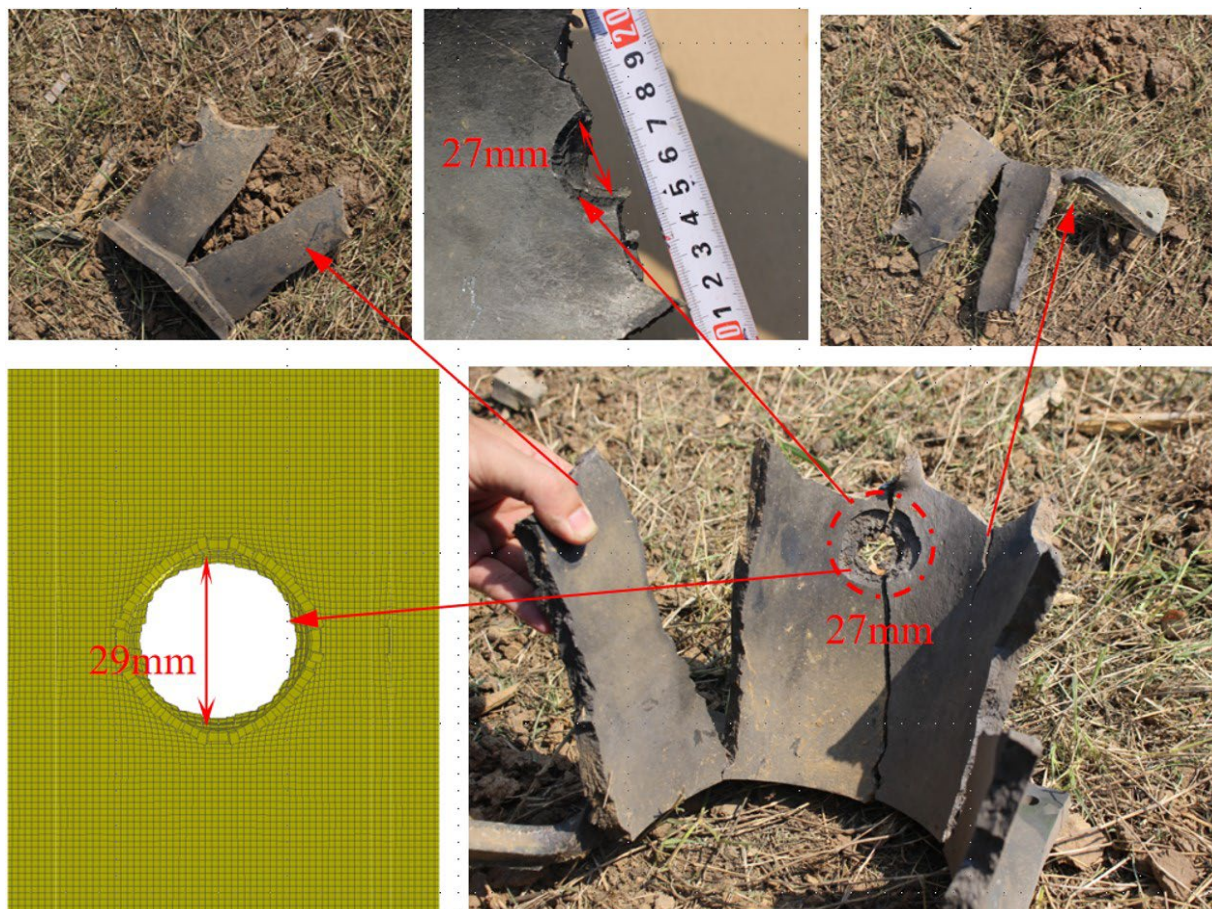
Figure 24: Comparison of recovered fragments with numerical simulation results

Numerical simulation and experimental study of the damage law of EFP warhead charging of cylindrical
shells under different angles

Kun Zhang et al.

5 CONCLUSION

In this study, the impact-initiation performance of an EFP warhead against a cylindrical-shell charge at different angles was studied. Through the experimental test and numerical simulation, the following conclusions were obtained:

1. The closer the charge-shell element is to the axis, the greater the impulse of the detonation wave is, while the farther the charge shell element is from the axis, the greater the impact is. By analyzing the ratio of the impulse received by the charge-type cover elements along the radial direction from the bottom, an exponential function with a correlation index of 0.9943 can be fitted, which shows that the impulse received by each element of the liner under the action of the detonation-wave decays in the radial direction in the form of an approximate exponential.

2. Under the conditions studied in this work, the EFP warhead does not have the optimal initiation ability in vertical penetration with cylindrical-shell charge. According to the radial-cylindrical elastic-wave theory and convergent-detonation theory, when the angle ϑ is within the range of [0°, 10°], the warhead impact-detonation efficiency is consistent with the change law of the stress amplitude of the cylindrical elastic wave σ_r, which shows a linear-growth relationship with $1/\sqrt{\cos\theta}$. With the increase of angle ϑ, the effect of tangential velocity v_y becomes obvious when the projectile impacts the shell. This indicates that the linear relationship between σ_r and $1/\sqrt{\cos\theta}$ is no longer established, and the impact-initiation efficiency of the warhead decreases significantly.

3. Under this calculation example, the EFP warhead has a strong impact-initiation ability when the impact angle of the warhead is within the range of 0°-30°. When the impact angle of the warhead is greater than 36°, the projectile cannot impact and detonate the cylindrical-shell charge. Finally, when the angle is greater than 40°, the projectile ricochets instead.

Acknowledgements

Author's Contributions: Conceptualization, Kun Zhang and Chong Ji; Investigation, Kun Zhang and Changxiao Zhao; Methodology, Kun Zhang and Shaoguang Zhang; Resources, Xin Wang and Tao Jiang; Supervision, Kun Zhang andGang Wu; Validation, Kun Zhang and Chong Ji; Writing – original draft, Kun Zhang and Changxiao Zhao; Writing – review & editing – Preparation, Kun Zhang, Chong Ji and Changxiao Zhao.

Editor: Pablo Andrés Muñoz Rojas

References

Cardoso D., Teixeira-Dias, F. (2016). Modelling The Formation of Explosively Formed Projectiles (EFP). International Journal of Impact Engineering, 93(), 116-127. doi:10.1016/j.ijimpeng.2016.02.014.

Castedo R., Santos A.,Yenes J., et al. (2018). Finite Elements Simulation of Improvised Explosively Formed Projectiles. Engineering Computations, https://doi.org/10.1108/EC-04-2017-0130.

Ding L, Jiang J W, Men J B,et al (2017). Research on Feasibility of Several High Density Materials for EFP Liner and Material Selection Criteria. Propellants, Explosives, Pyrotechnics, 42(4), 360-369. doi:10.1002/prep.201600141.

Guo C, Guo S S, Qian J P, et al (2020). Numerical Simulation on Shock Critical Initiation Velocity of Cylindrical Covered Charge by Multiple Fragment Impacts. EXPLOSION AND SHOCK WAVES. 2020,40(06):24-32.doi:10.11883/bzycj-2019-0391.(In Chinese)

Hallquist J O. (2007). LS-DYNA Theoretical Manual. Livermore Software Technology Corporation, Livermore, CA, USA.

Hong X W, Li W B; Li W B, et al (2019). Experimental Study on Explosion Dispersion Process of a Multi-layer Composite Charge Under Different Initiation Modes. Defence Technology, (), S2214914719306646–. doi:10.1016/j.dt.2019.11.002.

Hu F, Wu H, Fang Q, et al (2018). Impact Resistance of Concrete Targets Pre-damaged by Explosively Formed Projectile (EFP) Against Rigid Projectile. International Journal of Impact Engineering, (), S0734743X18306432-. doi:10.1016/j.ijimpeng.2018.08.014

Numerical simulation and experimental study of the damage law of EFP warhead charging of cylindrical
shells under different angles

Kun Zhang et al.

Jiang G P(2006) .Heterogeneous Explosives Experimentally Investigated and Analyzed by Lagrange Analysis Method in Two Demsions Production Process [D].Hunan University, Changsha, China.(In Chinese)

Lee,E.L., and C.M. Tarver. (1980) .Phenomenological Model of Shock Initiation in Heterogeneous Explosives. *Physics of Fluids* 23:2362–72. doi:10.1063/1.862940.

Li B,Chen X,Du Z H, et al (2016) .Numerical Simulation and Experimental Study of LEFP on Impact Initiation Process of Charge with Shell.Chinese of Energetic Materials,24(11):1034-1040.(In Chinese)

Li YM, Li W B, Zhang Q, et al (2020). Shock Initiation of Covered Flake JH-2 High Explosive by Simultaneous Impact of Multiple Fragments. Propellants Explosives Pyrotechnics, 45(1-9).doi:10.1002/prep.201900366.

Liang Z G, Chen B X; Nan Y X, et al (2019). Research on the computing method for the forming velocity of circumferential multiple explosive formed projectiles. The Journal of Defense Modeling and Simulation: Applications, Methodology, Technology, (), 154851291983318-. doi:10.1177/1548512919833187.

Liu J F, Long Y, Ji C, et al. (2017a). Dynamic Response and Microstructure Evolution of Oxygen-Free High-Conductivity Copper Liner in Explosively Formed Projectile. Latin American Journal of Solids and Structures, 14(11), 2089-2106. doi:10.1590/1679-78253958.

Liu J.F.,Long Y., Ji C., et al, (2017b). The Influence of Liner Material on the Dynamic Response of the Finite Steel Target Subjected to High Velocity Impact by Explosively Formed Projectile. International Journal of Impact Engineering 109:264-275.doi:10.1016/j.ijimpeng.2017.07.002.

Liu J, Chen X, Du Z H, (2020). A Study on The Surface Overpressure Distribution and Formation of a Double Curvature Liner under a Two-point Initiation. Defence Technology, (), S2214914720304621-. doi:10.1016/j.dt.2020.10.004.

Liu Y K, Yin JP, Wang ZJ, et al. (2020). The EFP Formation and Penetration Capability of Double-Layer Shaped Charge with Wave Shaper. Materials, 13(20), 4519-. doi:10.3390/ma13204519.

Long Y, Liu JF, Ji C, et al (2016). Numerical Simulation on Formation and Penetration of Double-layer Liners EFP Warhead Influenced by Multi-point Initiation. ACTA ARMAMENTARII,37(12):2226-2234.

Selberg H L (1952). Transient Compression of Waves from Spherical and Cylindrical Cavities.Arkiv for Fysik,5,97.doi:10.1016/0014-5793(87)80584-7.

Tang Y, Wu T F,Gu W B, et al (2004). Feasibility of BSW Initiating Explosive When EFP Penetrating Covered Explosive. Journal of PLA University of Science and Technology(Natural Science) Vol.5(1):73-75.

Tarver,C.M. (2016). Ignition and Growth Reactive Flow Model for IMX-101. LLNL-TR-683439. Livermore, CA, USA:Lawrence Livermore National Laboratory.

Timoshenko S,Goodier J N (1951) .Theory of Elasticity[M].New York:Mc Graw-Hill,1951:56-83.

Wang L L,Zhu Z X (2005). Foundation of Stress Waves[M]. Beijing,National Defence Industry Press,2005:216-239.(In Chinese)

Wu J;Liu J; Du Y X (2007). Experimental and Numerical Study on the Flight and Penetration Properties of Explosively Formed Projectile., International Journal of Impact Engineering. 34(7), 1147–1162. doi:10.1016/j.ijimpeng.2006.06.007.

Xu W L, Wang C, Chen DP (2019). Formation of a Bore-center Annular Shaped Charge and Its Penetration into Steel Targets. International Journal of Impact Engineering, 127(), 122-134.doi:10.1016/j.ijimpeng.2019.01.008.

Xu YX, Gao P, Wang SS (2017) .Critical Criterion for The Shock Initiation/Ignition of Cylindrical Charges with Thin Aluminum Shell Impacted by Steel Fragment. Propellants Explosives Pyrotechnics 42(8), 921-931.doi:10.1002/prep.201700081.

Yang Y,Han Y,Duan Y L, et al (2022) .Numerical Simulation of Cylindrical Charge Initiated by Simultaneous Impact of Two Fragments.ACTA ARMAMENTARII:1-9[2022-04-18].http://kns.cnki.net/kcms/detail/11.2176.TJ.20210913.2013.016.(In Chinese)

Zhang G R,Chen D N (1991).Dynamics of Initiation of Condensed Explosive[M].Beijing,National Defence Industry Press,1991:112-127.(In Chinese)

Zhu C S, Huang Z X, Zu X D, et al (2014). Mach wave control in explosively formed projectile warhead. Propellants, Explosives, Pyrotechnics;39(6):909-915.doi:10.1002/prep.201400106.

Numerical simulation and experimental study of the damage law of EFP warhead charging of cylindrical shells under different angles

Kun Zhang et al.

Zu X D, Huang Z X, Zhu C S, et al. (2016). Study of Detonation Wave Contours in EFP warhead. Defence Technology, 12(2), 129-133. doi:10.1016/j.dt.2016.01.002.